

## Research Article

# Inverted Metamorphic III–V Triple-Junction Solar Cell with a 1 eV CuInSe<sub>2</sub> Bottom Subcell

A. W. Walker, F. Bouchard, A. H. Trojnar, and K. Hinzer

SUNLAB, University of Ottawa, 800 King Edward Avenue, Ottawa, ON, Canada K1N 6N5

Correspondence should be addressed to A. W. Walker; [awalk102@uottawa.ca](mailto:awalk102@uottawa.ca)

Received 5 December 2013; Revised 7 May 2014; Accepted 16 May 2014; Published 9 July 2014

Academic Editor: Shinya Higashimoto

Copyright © 2014 A. W. Walker et al. This is an open access article distributed under the Creative Commons Attribution License, which permits unrestricted use, distribution, and reproduction in any medium, provided the original work is properly cited.

A new triple-junction solar cell (3J) design exploiting the highly absorptive I–III–VI chalcopyrite CuInSe<sub>2</sub> material is proposed as an alternative to III–V semiconductor 3J solar cells. The proposed structure consists of GaInP (1.9 eV)/Ga(In)As (1.4 eV)/CuInSe<sub>2</sub> (1 eV) which can be grown on a GaAs substrate in an inverted manner using epitaxial lift-off techniques. To lattice-match epitaxial CuInSe<sub>2</sub> to Ga(In)As, a compositionally graded buffer region composed of Ga<sub>x</sub>In<sub>1-x</sub>P is used. The modeling and simulation of the device include the effects of threading dislocations on minority carrier lifetimes in the metamorphic buffer and bottom subcell active region. Studies focus on device performance under standard testing conditions and concentrated illumination. The results are compared to a reference lattice mismatched 3J composed of GaInP (1.9 eV)/Ga(In)As (1.4 eV)/GaInAs (1 eV) and to a lattice matched 3J composed of GaInP (1.9 eV)/Ga(In)As (1.4 eV)/Ge (0.67 eV). The advantage of CuInSe<sub>2</sub> is its higher absorption coefficient, which requires only 1 μm of active material compared to 4 μm of GaInAs in the bottom subcell of the reference lattice mismatched cell. The proposed design reaches an efficiency of 32.6% under 1 sun illumination at 300 K with 10<sup>5</sup> cm<sup>-2</sup> threading dislocations and 39.6% at 750 suns.

## 1. Introduction

The area of research and development in photovoltaic device technologies has led to significant increases in power conversion efficiencies from 17% to 44.4% since 1983 [1]. The example of current state-of-the-art triple-junction solar cells (3Js) composed of III–V semiconductor materials is the bandgap engineered lattice matched (LM) Ga<sub>0.44</sub>In<sub>0.56</sub>P/Ga<sub>0.92</sub>In<sub>0.08</sub>As/Ge solar cell. This cell has achieved efficiencies greater than 40% under concentrated illumination [2] despite a nonoptimal bandgap of the germanium bottom subcell leading to a significant overproduction of photocurrent and thereby limiting the device's efficiency.

For more ideal current matching, a metamorphic lattice mismatched (LMM) 3J design composed of GaInP (1.9 eV)/Ga(In)As (1.4 eV)/Ga<sub>0.7</sub>In<sub>0.3</sub>As (1.0 eV) has been proposed [2], where the Ge bottom subcell has been replaced with the LMM ternary alloy Ga<sub>0.7</sub>In<sub>0.3</sub>As (hereafter referred to as GaInAs). To maintain high crystalline material quality, the device requires an inverted growth on a GaAs substrate

such that the formation of threading dislocations resulting from the LMM induced strain is confined within a compositionally graded buffer (CGB) region located away from the active regions of the middle and top subcells [3, 4]. Epitaxial lift-off techniques of the active regions of the device from the GaAs substrate also allow for the reuse of the substrate which further reduces the costs associated with this complex 3J design architecture.

Here we suggest a similar approach to integrate a lower cost epitaxial material CuIn<sub>1-x</sub>Ga<sub>x</sub>Se<sub>2</sub> (CIGS) as a bottom subcell in a 3J, as shown in Figure 1. To reach the desired bandgap of 1.0 eV for the bottom cell, the stoichiometry of the CIGS subcell must be close to  $x = 0$  or  $\alpha$ -CuInSe<sub>2</sub>, with ~25% Cu. The proposed epitaxial growth methods of chalcopyrite CuInSe<sub>2</sub> on a GaAs substrate with (001) orientation follow the methods described by Liao and Rockett using a hybrid cosputtering and coevaporation technique using two magnetron sputterers [5], whereas standard metal-organic chemical vapor deposition techniques are adopted for the III–V semiconductors. The design of the 3J is outlined in

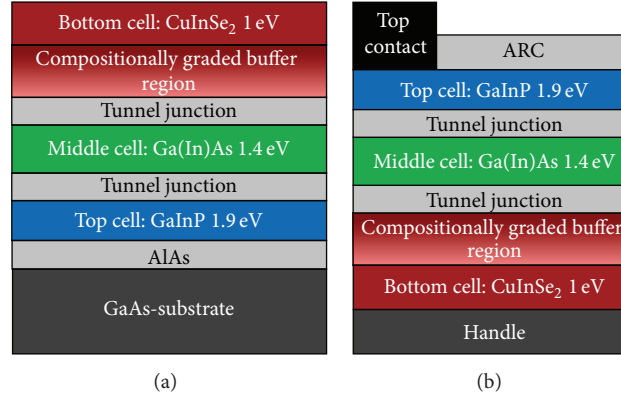


FIGURE 1: Proposed (a) growth sequence and (b) final design of the inverted metamorphic GaInP/Ga(In)As/CuInSe<sub>2</sub> structure after a selective wet etch of an AlAs release layer.

Layer name	Thickness (nm)	Doping (cm <sup>-3</sup> )
<i>n</i> -AlInPFSF	50	$1 \times 10^{19}$
<i>n</i> -GaInP emitter	40	$2 \times 10^{18}$
<i>i</i> -GaInP	300	$1 \times 10^{16}$
<i>p</i> -GaInP base	950	$1 \times 10^{17}$
<i>p</i> -AlGaInPBSF	100	$1 \times 10^{18}$
<i>p/n</i> -AlGaAs/AlGaAs TJ	60	$2 \times 10^{19}/2 \times 10^{19}$
<i>n</i> -GaInPFSF	30	$5 \times 10^{18}$
<i>n</i> -Ga(In)As emitter	70	$3 \times 10^{18}$
<i>i</i> -Ga(In)As	500	$5 \times 10^{15}$
<i>p</i> -Ga(In)As base	1900	$1 \times 10^{17}$
<i>p</i> -GaInPBSF	100	$1 \times 10^{19}$
<i>p/n</i> -AlGaAs/GaAs TJ	60	$2 \times 10^{19}/2 \times 10^{19}$
<i>n</i> -GaInAs buffer	200	$1 \times 10^{18}$
<i>n</i> -Ga <sub>0.51</sub> In <sub>0.49</sub> P CGB-1	250	$5 \times 10^{15}$
<i>n</i> -Ga <sub>0.47</sub> In <sub>0.53</sub> P CGB-2	250	$5 \times 10^{15}$
<i>n</i> -Ga <sub>0.43</sub> In <sub>0.57</sub> P CGB-3	250	$5 \times 10^{15}$
<i>n</i> -Ga <sub>0.39</sub> In <sub>0.61</sub> P CGB-4	250	$5 \times 10^{15}$
<i>n</i> -Ga <sub>0.35</sub> In <sub>0.65</sub> P CGB-5	250	$5 \times 10^{15}$
<i>n</i> -Ga <sub>0.31</sub> In <sub>0.69</sub> P CGB-6	250	$5 \times 10^{15}$
<i>n</i> -Ga <sub>0.27</sub> In <sub>0.73</sub> P CGB-7	250	$5 \times 10^{15}$
<i>n</i> -Ga <sub>0.22</sub> In <sub>0.78</sub> P overshoot	1000	$5 \times 10^{15}$
<i>n</i> -Ga <sub>0.25</sub> In <sub>0.75</sub> P	250	$5 \times 10^{15}$
<i>n</i> -GaInAs emitter	100	$1 \times 10^{18}$
<i>p</i> -CuInSe <sub>2</sub> base	1000	$1 \times 10^{16}$
<i>p</i> -CuInSe <sub>2</sub> BSF	100	$1 \times 10^{18}$

FIGURE 2: Structural details of the inverted metamorphic GaInP/Ga(In)As/CuInSe<sub>2</sub> structure.

Figure 2 and consists of a top GaInP subcell, with the middle Ga(In)As and bottom CuInSe<sub>2</sub> subcells interconnected by tunnel junctions (TJ).

The aim of this paper is to investigate the potential benefits of this material system as the third subcell of a 3J for

concentrated photovoltaic (CPV) applications using TCAD Sentaurus by Synopsys version vG-2012 (Mountain View, California) [6]. As demonstrated in this paper, a key advantage of replacing the GaInAs (1 eV) as bottom subcell with CuInSe<sub>2</sub> with the same bandgap is a reduction of  $\sim 20\%$  in total cell material thickness, and the cheaper cost of the chalcopyrite elements compared to GaInAs. This work is a continuation of our numerical modeling work on CIGS solar cells [7].

The paper is outlined as follows. Section 2 discusses the growth considerations of integrating III-V and I-III-VI semiconductors, including details of the proposed structure. Section 3 outlines the important properties of the relevant materials and describes models of CGB region and the GaInAs/CuInSe<sub>2</sub> interface based on threading dislocations and surface recombination, respectively. Section 4 then focuses on the simulation results of the proposed 3J under both standard testing conditions and concentrated illumination at 300 K. The simulation results are compared to the aforementioned LMM and LM 3Js, whose structures are described in Sections 2.2 and 2.3 respectively. Section 5 then gives the conclusions and implications of this study.

## 2. Structures

**2.1. CuInSe<sub>2</sub> 3J.** The growth of epitaxial CuInSe<sub>2</sub> on GaAs has been demonstrated previously in the literature for photovoltaic applications [9, 10] and in an effort to improve the understanding of the fundamental properties of epitaxial CuInSe<sub>2</sub> [11, 12]. In [10], a CuInSe<sub>2</sub> single junction solar cell epitaxially grown on a GaAs substrate was reported to achieve an efficiency of 6.3%. A possible reason for the low power conversion efficiency reported is the lattice mismatch between GaAs and CIGS, which induced the interdiffusion of Ga into CIGS. This resulted in a strong increase in Ga content near GaAs/CIGS interface. The quality of CIGS with such stoichiometries has been argued to induce significant levels of nonradiative recombination as a result of defects with a wide range of energies within the bandgap [8, 13–15]. To avoid the formation of Ga rich CIGS, we propose to introduce a CGB

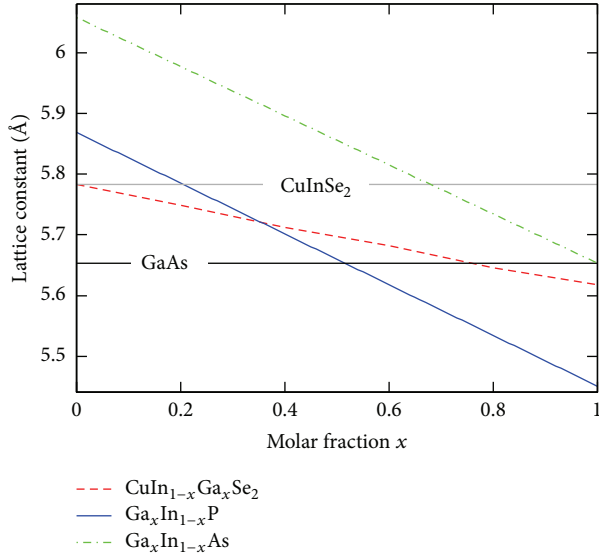


FIGURE 3: Lattice constant as a function of molar fraction for  $\text{CuIn}_{1-x}\text{Ga}_x\text{Se}_2$ ,  $\text{Ga}_x\text{In}_{1-x}\text{P}$ , and  $\text{Ga}_x\text{In}_{1-x}\text{As}$  based on [8].

region composed of III-V semiconductors to lattice match GaAs to  $\text{CuInSe}_2$ .

A candidate for the CGB material is the ternary alloy  $\text{Ga}_x\text{In}_{1-x}\text{As}$  based on its ability to be grown with high quality as demonstrated in the LMM GaInP/Ga(In)As/Ge cell [3]. However, it would not be optically transparent for the  $\text{CuInSe}_2$  subcell in the proposed 3J cell. The quaternary alloy AlInGaAs has been also discussed as a CGB [16]; however, it has been shown to be difficult to grow with high quality, and the optical and electrical properties for this material have not been thoroughly reported in the literature. Therefore, the proposed bottom  $\text{CuInSe}_2$  subcell design consists of an  $n$ -type CGB region composed of the high bandgap material  $\text{Ga}_x\text{In}_{1-x}\text{P}$ . The growth of 7 layers of a  $\text{Ga}_x\text{In}_{1-x}\text{P}$  CGB region has been successfully demonstrated in a 3J with misfit dislocations localized within the CGB region with densities below  $1 \times 10^6 \text{ cm}^{-2}$  [4]. A  $1 \mu\text{m}$  overshooting layer composed of  $\text{Ga}_{0.25}\text{In}_{0.75}\text{P}$  was grown on the 7 CGB layers for the active region of the bottom subcell to remain nearly defect free [17].

The details of the structure are outlined in Figure 2, and the relevant material lattice constants are depicted in Figure 3 as a function of their respective molar fractions [18]. The structure consists of a top GaInP (1.9 eV) subcell in an  $n$ - $i$ - $p$  homojunction configuration with the higher bandgap quaternary alloy  $(\text{Al}_{1-x}\text{Ga}_x)_{0.51}\text{In}_{0.49}\text{P}$  forming front and back surface fields (FSF and BSF, resp.). A high bandgap  $\text{Al}_{0.3}\text{Ga}_{0.7}\text{As}/\text{Al}_{0.3}\text{Ga}_{0.7}\text{As}$  tunnel junction (TJ) then interconnects the top subcell to an Ga(In) As  $n$ - $i$ - $p$  subcell [19, 20]. Similarly, an  $\text{Al}_{0.3}\text{Ga}_{0.7}\text{As}/\text{GaAs}$  TJ interconnects the middle GaInAs to the  $\text{Ga}_x\text{In}_{1-x}\text{P}$  CGB layers (as described above) followed by a bottom  $n$ - $p$  heterojunction. The bottom subcell in the proposed design would consist of  $n$ - $\text{In}_{0.3}\text{Ga}_{0.7}\text{As}$  and a  $p$ -type base composed of  $\text{CuInSe}_2$  with a  $\text{CuInSe}_2$  back surface field equivalently doped to  $1 \times 10^{18} \text{ cm}^{-3}$ ; the doping of  $\text{CuInSe}_2$  to such levels has been demonstrated previously

[11]. A selective wet etch and lift-off technique can be used to detach the GaAs substrate from the top GaInP subcell using hydrofluoric acid by dissolving an AlAs release layer (see Figure 1) [21]. The stack of III-V semiconductor layers including the  $\text{CuInSe}_2$  bottom subcell can be bonded to a deposited on a flexible handle prior to lift off for subsequent solar cell device fabrication and processing using standard photolithography and metal deposition techniques. A highly doped GaAs cap layer is used to make an ohmic top contact with the top subcell and an Au/Ti bottom contact for contacting to the  $\text{CuInSe}_2$  subcell. A dual layered broadband antireflection coating (ARC) composed of  $\text{MgF}_2/\text{TiO}_x$  is deposited on the structure to minimize incident light reflection ( $0.1 \mu\text{m}/0.06 \mu\text{m}$  thick resp.).

**2.2. GaInAs LMM 3J.** The reference LMM 3J is composed of GaInP (1.9 eV)/Ga(In)As (1.4 eV)/GaInAs (1 eV) and is identical to the structure in Figure 2 with the exception of the bottom subcell active region which is composed of  $\text{Ga}_{0.7}\text{In}_{0.3}\text{As}$  (1 eV) with a  $4 \mu\text{m}$  base for current matching. The BSF composed of  $\text{Ga}_{0.25}\text{In}_{0.75}\text{P}$  is used, since a highly doped GaInAs BSF resulted in a poor  $FF$  of the device under high concentration. The top and middle subcell base thicknesses are optimized to obtain the highest efficiency, and the top subcell bandgap is set to 1.9 eV. The details of the CGB are also identical to Figure 2 to allow for a better device comparison to the  $\text{CuInSe}_2$  3J.

**2.3. Ge LM 3J.** Similarly, the LM design composed of GaInP (1.9 eV)/Ga(In)As (1.4 eV)/Ge (0.67 eV) is identical to Figure 2 for the top and middle subcells with the exception of their base thicknesses (based on current matching). Furthermore, no CGB is required for the bottom Ge subcell. Instead, the Ge subcell is composed of a  $\text{Ga}_{0.99}\text{In}_{0.01}\text{As}$  buffer layer followed by a  $\text{Ga}_{0.51}\text{In}_{0.49}\text{P}$  FSF and a Ge homojunction on a Ge substrate.

### 3. Numerical Model

**3.1. Model.** The semiconductor simulation software TCAD Sentaurus is used to specify the 3J structure of interest and solve the set of coupled differential equations consisting of Poisson's equation and the electron and hole current-continuity equations with thermionic emission as boundary conditions for heterointerfaces. These equations consider generation computed using the transfer matrix method, and radiative, Shockley-Read-Hall and Auger recombination using standard recombination formalisms [6]; surface recombination is implemented at the relevant heterointerfaces and is discussed in more detail in Section 3.3. The tunnel junctions are modeled based on [19, 20]. Details on the numerical modeling environment and its applications to 3J can be found elsewhere [7, 19, 20, 22, 23].

**3.2. Material Properties.** The most important properties for CIGS and  $\text{Ga}_x\text{In}_{1-x}\text{P}$  as a function of molar fraction include (1) the bandgap and electron affinity at room temperature, (2) the optical properties in terms of refractive index and

TABLE 1: Material properties for  $\text{CuIn}_{1-x}\text{Ga}_x\text{Se}_2$  and  $\text{Ga}_x\text{In}_{1-x}\text{P}$ .

Parameter	Model for $\text{CuIn}_{1-x}\text{Ga}_x\text{Se}_2$	Model for $\text{Ga}_x\text{In}_{1-x}\text{P}$
$E_g$ (eV)	$1.01 + 0.626x - 0.167x(1-x)$ [24]	$1.34 + 1.44x - 0.65x(1-x)$ [25]
$\chi$ (eV)	$4.35 - 0.421x - 0.244x^2$ [26]	$4.38 - 0.58x$ [18]
$\epsilon_r$	$15.1 - 5x$ [27]	$12.5 - 1.4x$ [18]
$N_c, N_v$ ( $\text{cm}^{-3}$ )	$2.2 \times 10^{18}, 1.8 \times 10^{19}$ [28]	[29]
$\mu_e, \mu_h$ ( $\text{cm}^2/\text{Vs}$ )	300, 200 [11]	[30]
$\tau_e^{\text{SRH}}, \tau_h^{\text{SRH}}$ (ns)	3, 3 [31]	20, 20 [32]
$n, k$	[33]	[34]

extinction coefficient, (3) carrier mobilities, and (4) minority carrier recombination lifetimes. The radiative recombination coefficient  $B_{\text{rad}}$  for CIGS is set to  $10^{-14} \text{ cm}^3/\text{s}$  such that the material is dominated by non-radiative processes. For GaInP in the CGB region,  $B_{\text{rad}}$  is assumed constant over molar fraction based on data for  $\text{Ga}_{0.51}\text{In}_{0.49}\text{P}$  [32] since the CGB region is a majority carrier region, and thus the recombination in these layers is not relevant to device performance. In any event, SRH recombination would dominate due to the effects of threading dislocations. The parameters adopted in the simulations for CIGS and GaInP are summarized in Table 1, where a molar fraction-dependent expression for carrier mobilities is developed for GaInP based on interpolation schemes for  $x = 0, 0.51$ , and 1 using data from [30]. The material properties for the remaining III-V semiconductor materials can be found elsewhere [23], with the specific data for GaInAs obtained from the literature for bandgap [35], electron affinity [35], effective density of states [18], carrier mobilities [30], optical data based on interpolation between GaAs [34] and InAs [36], and lastly, minority carrier recombination lifetimes for radiative [37], for Shockley-Read-Hall [38], and for Auger [18]. It is assumed that carrier mobilities are not significantly influenced by threading dislocations for densities below  $10^8 \text{ cm}^{-2}$  [39].

**3.3. Modeling the Compositionally Graded Buffer Region and the Relevant Interface.** The energy band diagram of the complete  $\text{CuInSe}_2$  3J structure simulated at equilibrium is shown in Figure 4(a). The structure of the cell consisting of the top GaInP subcell, middle InGaAs subcell, layers of  $\text{Ga}_x\text{In}_{1-x}\text{P}$  CGB, and overshoot layer (marked in gray) as well as bottom subcell (InGaAs emitter and  $\text{CuInSe}_2$  base) are denoted above the band diagram.

A closeup of the bottom subcell is shown in Figure 4(b) which shows 7 CGB layers and the overshoot layer based on [17]. The background doping of the CGB is set to  $5 \times 10^{15} \text{ cm}^{-3}$  as a representation of a realistic unintentional background doping, although the device shows no dependence on this doping level under standard testing conditions. The mesh density in these layers is set to be sufficiently large to resolve the appropriate current transport phenomena. Minimal band offsets are present at the GaInAs/ $\text{CuInSe}_2$  interface due to the similar electron affinities and bandgaps based on typical heterostructure band alignment considerations. No bandgap narrowing is considered in the model for  $\text{CuInSe}_2$ .

The effects of threading dislocations on current transport are also considered in the model by effectively modifying the minority carrier Shockley-Read-Hall (SRH) lifetimes parameterized by the threading dislocation density (TDD), as described in [40] and adopted in [41] to model a III-V semiconductor based 3J grown on a Si substrate. The modified SRH lifetime can be expressed as

$$\frac{1}{\tau_{\text{SRH},\text{TDD}}} = \frac{1}{\tau_{\text{SRH}}} + \frac{\pi^3 D [\text{TDD}]}{4}, \quad (1)$$

where  $D$  is the diffusion coefficient which considers the doping dependent mobility of the material through the Einstein relation,  $\tau_{\text{SRH}}$  is the doping-dependent SRH recombination lifetime with no TDD affects (see Table 1), and  $[\text{TDD}]$  is the threading dislocation density in units of  $\text{cm}^{-2}$ . In both  $\text{CuInSe}_2$  and LMM 3J structures, the effects of TDDs are considered in both the CGB ( $\text{TDD}_{\text{CGB}}$ ) and the active region of bottom cell ( $\text{TDD}_{\text{bot}}$ ). Since LM 3J is lattice matched it is assumed that there is minimal formation of TDD in this structure. The effective lifetimes for carriers in  $\text{CuInSe}_2$  and for GaInAs are illustrated in Figure 5 as a function of TDD, where a threshold density is defined as one which reduces the effective lifetime by a factor of 2.

Lastly, each interface of the complete structure considers surface recombination which is parameterized using a surface recombination velocity (SRV) according to the standard interface recombination formalism [6]. Lattice matched interfaces are assumed to have  $\text{SRV} < 10^3 \text{ cm/s}$  due to minimal strain and ideal growth conditions. However, the quality of the CGB is expected to affect the GaInAs/ $\text{CuInSe}_2$  interface quality, and a SRV is also associated with this interface. To reduce the parameter space of this study and to target an ideal yet realistic lattice matched interface quality, a fixed surface recombination velocity of  $10^3 \text{ cm/s}$  is implemented for the GaInAs/ $\text{CuInSe}_2$  interface of the  $\text{CuInSe}_2$  3J and for the GaInAs/GaInAs interface of the LMM 3J. However, note that the interface recombination occurring within the CGB region is not important since majority carriers dominate the transport.

## 4. Simulation Results

**4.1. Standard Testing Conditions.** The simulated external quantum efficiency (EQE) and current-voltage ( $J$ - $V$ ) characteristics of the  $\text{CuInSe}_2$  based 3J are illustrated in Figures 6(a) and 6(b), respectively, for increasing levels of

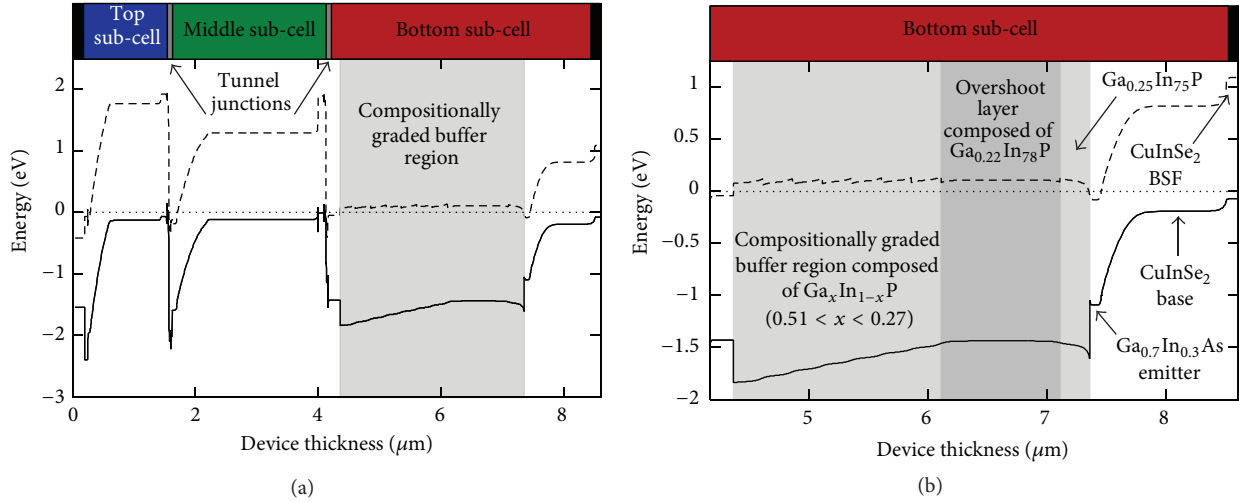


FIGURE 4: (a) Simulated energy band diagram of the GaInP/Ga(In)As/CuInSe<sub>2</sub> 3J under illumination conditions and (b) a closeup of the energy band diagram at the compositionally graded buffer region composed of GaInP including the overshoot layer and the CuInSe<sub>2</sub> based bottom subcell including a highly doped CuInSe<sub>2</sub> back surface field (BSF).

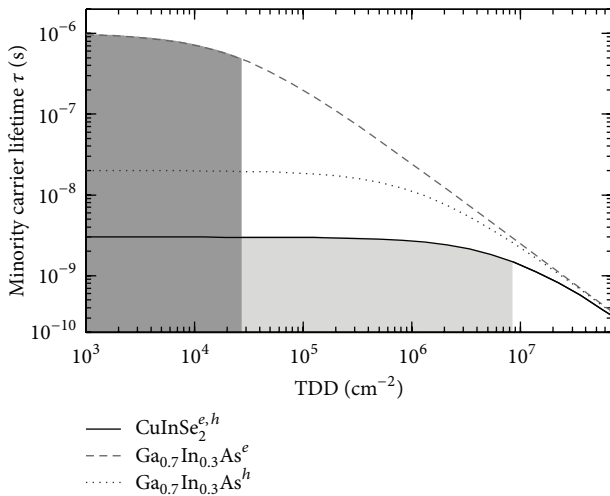


FIGURE 5: Minority carrier lifetimes in CuInSe<sub>2</sub> and GaInAs as a function of threading dislocation densities (TDD). A threshold density of  $8.4 \times 10^6 \text{ cm}^{-2}$  for CuInSe<sub>2</sub> can be observed based on the reduction of the lifetime by a factor of 2 (marked by light gray rectangle), whereas the threshold is closer to  $2.6 \times 10^4 \text{ cm}^{-2}$  for electrons in GaInAs (marked by dark gray rectangle).

TDD in the bottom subcell. The  $\text{TDD}_{\text{CGB}}$  is fixed to  $10^6 \text{ cm}^{-2}$  although this has no influence on the performance of the device because transport is a majority carrier phenomenon. For comparison, the  $J$ - $V$  characteristics for the simulated LM and LMM 3Js are also included, the latter calculated with  $\text{TDD}_{\text{CGB}} = 10^6 \text{ cm}^{-2}$  and a  $\text{TDD}_{\text{bot}} = 10^5 \text{ cm}^{-2}$  in the active bottom subcell to outline near-ideal characteristics. The AM1.5D spectrum is normalized to  $1000 \text{ W cm}^{-2}$  scaled from the ASTM G173-03.

The EQE of the top GaInP subcell has a comparable albeit high response in the UV to other published data [42], with

its squareness in the long wavelength range attributed to its optically thick base. The absorption range of the top subcell is limited by the bandgap close to 650 nm ( $E_g = 1.9 \text{ eV}$ ). The high response in the UV is due primarily to surface recombination at the top interfaces of the GaInP subcell ( $\sim 10^6 \text{ cm/s}$ ), in agreement with Haas et al. [29]. Doping-dependent SRH minority carrier lifetime parameters can provide further calibration of the top subcell EQE in terms of agreement with experiment. The  $n$ - $i$ - $p$  design of the top subcell coupled to the low reflectivity of the ARC allows for a large carrier collection probability, or in other words, a magnitude in EQE ( $>90\%$ ). Similarly, the middle Ga(In)As subcell EQE is large in magnitude due to its  $n$ - $i$ - $p$  design and low reflectivity. Its EQE is nonzero primarily in the wavelength range of 650 to 880 nm and corresponds to the bandgaps of GaInP (1.9 eV) and Ga(In)As (1.4 eV). One can observe the minimal current sharing between the top and middle subcells. However, the middle subcell base is designed to share photons with the bottom CuInSe<sub>2</sub> subcell to enhance the overall device fill factor since the CuInSe<sub>2</sub> individual subcell's  $FF$  is low (69%). Only  $1 \mu\text{m}$  of active CuInSe<sub>2</sub> is required to obtain a photocurrent of  $15 \text{ mA/cm}^2$  and drops for larger base thicknesses due to etalon effects within this subcell. The EQE of the bottom CuInSe<sub>2</sub> sub-cell ranges from the Ga(In)As bandgap and its own (1.0 eV). As the  $\text{TDD}_{\text{bot}}$  is increased beyond a threshold density of  $10^6 \text{ cm}^{-2}$ , the EQE of the CuInSe<sub>2</sub> subcell decreases as it is the only subcell affected. It degrades by up to 30% absolute in the long wavelength region as seen in Figure 6(a) for a  $\text{TDD}_{\text{bot}} = 10^7 \text{ cm}^{-2}$ . This drop corresponds to half the minority carrier lifetime (see Figure 5).

Interestingly, one can notice on the  $J$ - $V$  curves outlined in Figure 6(b) that the  $J_{\text{sc}}$  of CuInSe<sub>2</sub> 3J remains constant for increasing  $\text{TDD}_{\text{bot}}$  up to  $10^7 \text{ cm}^{-2}$ . The lack of degradation of this metric is due to the shunt-like behavior of the CuInSe<sub>2</sub> subcell in reverse bias. The photocurrent of

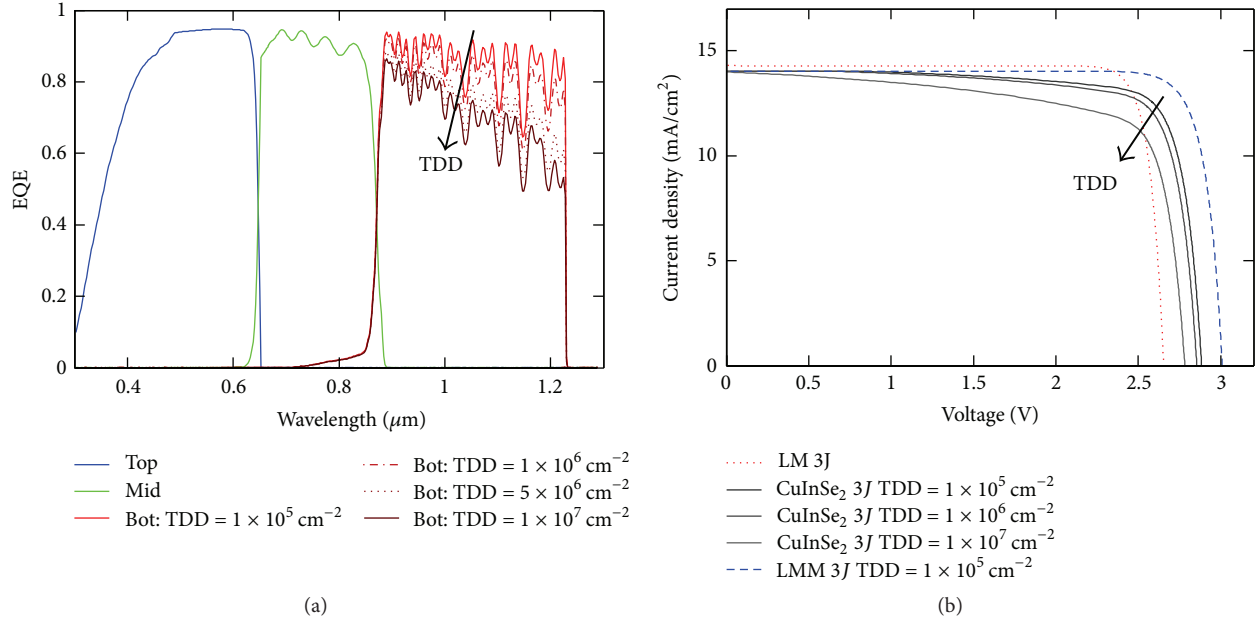


FIGURE 6: (a) Simulated EQE and (b)  $J$ - $V$  characteristics of the  $\text{CuInSe}_2$  3J for increasing levels of  $\text{TDD}_{\text{bot}}$  in the bottom subcell at  $1000 \text{ W/m}^2$  intensity and  $300 \text{ K}$ ; a fixed  $\text{TDD}_{\text{CGB}}$  of  $10^6 \text{ cm}^{-2}$  is adopted with SRV of  $10^3 \text{ cm/s}$  at the relevant CGB interfaces. The  $J$ - $V$  characteristics of the LMM and LM devices are shown for comparison, with the LMM device having a  $\text{TDD}_{\text{bot}} = 10^5 \text{ cm}^{-2}$  in the active region but a  $\text{TDD}_{\text{CGB}} = 10^6 \text{ cm}^{-2}$ .

TABLE 2: Simulated current-voltage metrics of the 3Js of interest under  $1000 \text{ W/m}^2$  and at  $300 \text{ K}$  with  $\text{TDD}_{\text{CGB}}$  and  $\text{TDD}_{\text{bot}}$  of  $10^6 \text{ cm}^{-2}$ .

3J structure	$J_{\text{sc}}$ ( $\text{mA/cm}^2$ )	$V_{\text{oc}}$ (V)	$FF$ (%)	$\eta$ (%)
$\text{CuInSe}_2$	14.0	2.86	79.0	31.7
LMM	14.0	2.95	83.2	34.5
LM	14.3	2.65	87.0	33.0

the device is thus maintained for increasing  $\text{TDD}_{\text{bot}}$  with a significant degradation in both  $V_{\text{oc}}$  and  $FF$  as a result of the bottom subcell being internally reverse biased. The increased SRH recombination occurring in the bottom subcells of the  $\text{CuInSe}_2$  and LMM 3J designs as the  $\text{TDD}_{\text{bot}}$  increase also strongly impacts their respective performance metrics due to the shorter minority carrier lifetime (see Section 3.3). Though not included, the EQE of the LMM device degrades in a similar fashion to the  $\text{CuInSe}_2$  3J for increasing  $\text{TDD}_{\text{bot}}$ . The performance metrics of each design are summarized in Table 2 for a fixed  $\text{TDD}_{\text{bot}}$  of  $10^6 \text{ cm}^{-2}$ .

Figures 7(a)–7(d) illustrate the  $J$ - $V$  metrics ( $J_{\text{sc}}$ ,  $V_{\text{oc}}$ ,  $FF$  and  $\eta$ ) for the  $\text{CuInSe}_2$  3J compared to those of the LMM and LM 3J devices as a function of  $\text{TDD}_{\text{bot}}$ . The results for the LM 3J  $J$ - $V$  metrics are constant as a function of  $\text{TDD}_{\text{bot}}$  since no TDD is considered in the structure assuming ideal strain management. The photocurrent of the  $\text{CuInSe}_2$  3J demonstrates a deterioration of 1.9% absolute over the complete range of  $\text{TDD}_{\text{bot}}$  studied, in agreement with the results from Figure 6(b). Comparatively, the photocurrent of the LMM

device degrades 16.7% since its bottom GaInAs subcell does not have the same shunt-like behavior as the  $\text{CuInSe}_2$  subcell. The LM device has a 1.8% higher photocurrent than the other two 3Js since there is less current sharing to the Ge subcell. On the other hand, the  $\text{CuInSe}_2$  and LMM 3Js have a higher top subcell bandgap for more optimal current matching considerations in an effort to maximize each device's fill factor.

With respect to the open circuit voltage, Figure 7(b) illustrates a strong degradation for both the  $\text{CuInSe}_2$  and LMM 3Js beyond their respective threshold densities of  $10^6 \text{ cm}^{-2}$  and  $3 \times 10^4 \text{ cm}^{-2}$ , since the SRH recombination increases inversely with the minority carrier lifetime (see Figure 5). The respective threshold TDDs are primarily dependent on the bulk SRH lifetime of the material. For the  $\text{CuInSe}_2$  3J, increasing the  $\text{TDD}_{\text{bot}}$  from  $10^6 \text{ cm}^{-2}$  to  $7 \times 10^7 \text{ cm}^{-2}$  results in a 5.8% absolute drop in  $V_{\text{oc}}$ , whereas the LMM device's  $V_{\text{oc}}$  degrades by 9.3% from  $10^4 \text{ cm}^{-2}$  to  $7 \times 10^7 \text{ cm}^{-2}$ . For the same  $\text{TDD}_{\text{bot}}$  of  $10^6 \text{ cm}^{-2}$ , the LMM 3J has a  $V_{\text{oc}}$  that is 3.1% higher than the  $\text{CuInSe}_2$  3J device and 11% higher than the LM 3J device (see Table 2).

The  $FF$  and  $\eta$  of both devices are constant up to each device's respective threshold  $\text{TDD}_{\text{bot}}$ , after which these metrics begin to degrade significantly as observed in Figures 7(c)–7(d). Interestingly, the LMM 3J illustrates two  $\text{TDD}_{\text{bot}}$  ranges where the  $FF$  decreases at different rates. These two ranges correspond to the two threshold densities for the electron and hole minority carrier lifetimes as illustrated in Figure 5. The  $FF$  of the  $\text{CuInSe}_2$  is the lowest of all devices over all  $\text{TDD}_{\text{bot}}$  explored, whereas the  $FF$  of the LM 3J is the highest. Under standard testing conditions, the proposed

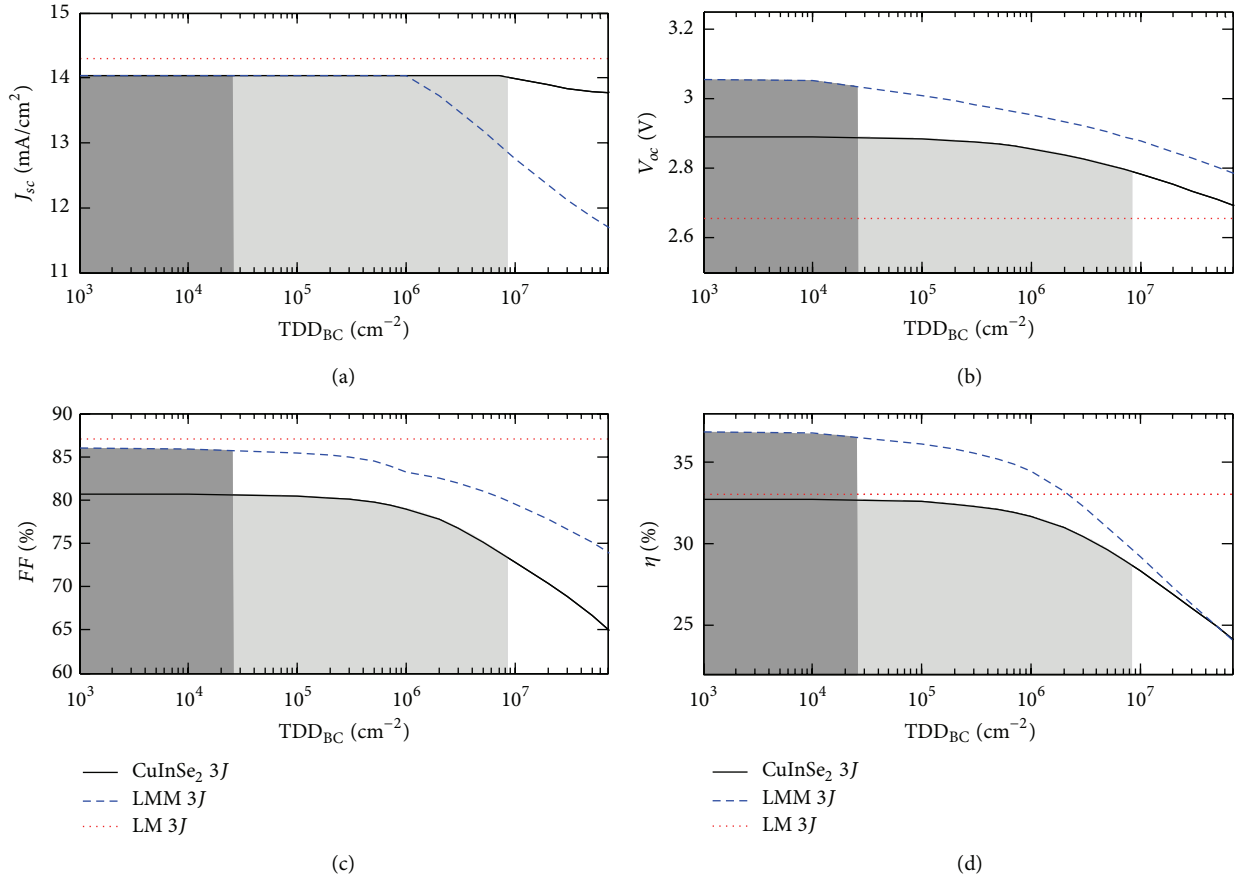


FIGURE 7: Simulated (a)  $J_{sc}$ , (b)  $V_{oc}$ , (c)  $FF$  and (d)  $\eta$  as a function of threading dislocation densities  $TDD_{bot}$  in the active region of the bottom subcell with  $TDD_{CGB} = 10^6 \text{ cm}^{-2}$  and surface recombination velocities of  $1 \times 10^3 \text{ cm/s}$  at the GaInAs/CuInSe<sub>2</sub> interface as well as each CGB interface, illuminated by the AM1.5D spectrum ( $1000 \text{ W/m}^2$ ) at 300 K. The light and dark gray regions indicate the threshold level of  $TDD_{bot}$  for the CuInSe<sub>2</sub> and LMM devices, respectively, for a reduction in minority carrier lifetime by a factor of 2.

3J composed of CuInSe<sub>2</sub> has the potential of converting the AM1.5D incident spectrum to electricity with an efficiency of 32.7% at 300 K with a  $FF$  of 80.7%, a photocurrent of  $14.0 \text{ mA/cm}^2$ , and an open circuit voltage of 2.89 V if there are no threading dislocations. If the threading dislocations in the bottom subcell reach a density of  $10^6 \text{ cm}^{-2}$ , the efficiency of this cell drops to 31.7% with  $FF$  of 79%. Comparatively, the LMM 3J can perform up to 34.5% assuming a  $TDD_{bot}$  of  $10^6 \text{ cm}^{-2}$ , whereas the LM 3J reaches 33.0% as it is free from any TDD effects (see Table 2).

The benefits of replacing a Ge subcell with an epitaxial CuInSe<sub>2</sub> subcell would thus enable a comparable efficiency at 1 sun operation compared to the LM device. With respect to the LMM device; however, a reduction in efficiency is observed due to the low  $FF$  of the CuInSe<sub>2</sub> subcell compared to the GaInAs subcell. This could be improved with a longer minority carrier lifetime in CuInSe<sub>2</sub>. However, an advantage of both the CuInSe<sub>2</sub> and LMM devices over the LM device is the reuse of the GaAs substrate for epitaxial growth through the exploitation of the aforementioned epitaxial lift-off process. For the case of the CuInSe<sub>2</sub> device, the growth process requires two chambers.

**4.2. Performance under Concentrated Illumination.** The simulated device  $V_{oc}$ ,  $FF$ , and efficiency are illustrated in Figures 8(a)–8(c) for the three aforementioned 3Js under concentrated illumination up to  $X = 3000$  suns where the temperature is kept fixed at 300 K. No contact series resistance is modeled in the simulation. The TDD parameters of each 3J are set to  $TDD_{CGB} = 10^6 \text{ cm}^{-2}$  and  $TDD_{bot} = 10^5 \text{ cm}^{-2}$  as an ideal scenario of optimized epitaxial growth with minimal formation of threading dislocations. The  $J_{sc}$  of each 3J is not shown here as it is linear as a function of  $X$ . As expected based on the results of Figures 6(b) and 7(b), the  $V_{oc}$  is largest for the LMM 3J over all concentrations with  $V_{oc} = 3.6 \text{ V}$  at  $X = 1000$ . Comparatively, the LM 3J has the smallest  $V_{oc}$  (3.2 V at  $X = 1000$ ), and the  $V_{oc}$  for the CuInSe<sub>2</sub> based 3J is only 2.7% lower than the LMM device at 1000 suns.

The  $FF$  for each of the 3Js is illustrated in Figure 8(b) and demonstrates trends that agree with those of Figure 7. The LM 3J has the largest device  $FF$  due to the bottom Ge subcell having the highest photocurrent compensating for its low individual  $FF$  of 63%. The LMM 3J has the second largest  $FF$  since it has the second highest bottom subcell photocurrent, even though its bottom subcell has the highest individual  $FF$  of 80%. The overall  $FF$  of CuInSe<sub>2</sub> 3J is

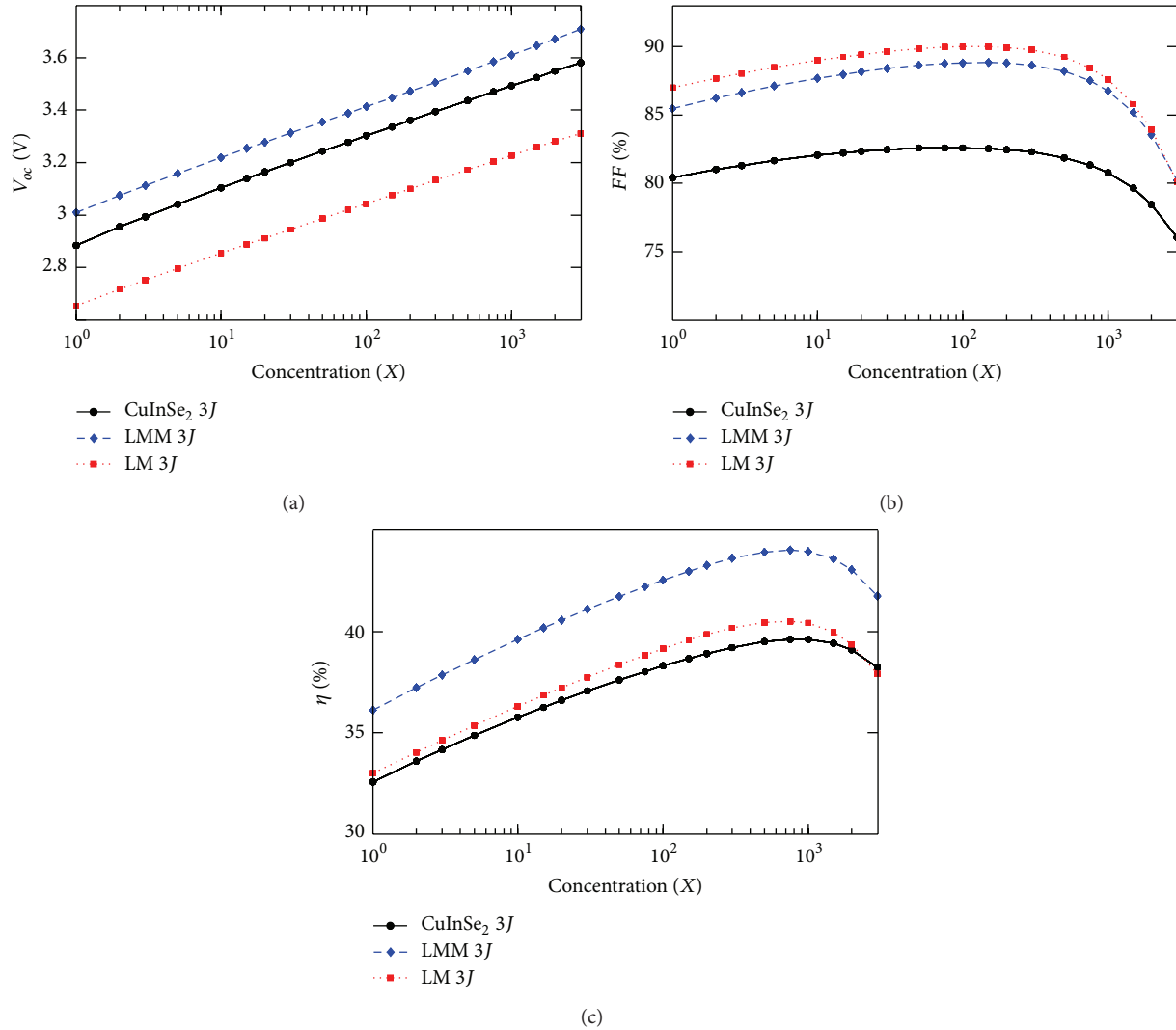


FIGURE 8: Simulated (a)  $V_{oc}$ , (b)  $FF$ , and (c) efficiency of the CuInSe<sub>2</sub> 3J at 300 K as a function of the concentrated illumination ratio ( $X$ ) for  $TDD_{bot} = 10^5 \text{ cm}^{-2}$  and surface recombination velocities of  $10^3 \text{ cm/s}$ . The simulated data is compared to the predicted performance of the LMM 3J with the same TDD and to the LM 3J.

the lowest of all three devices since CuInSe<sub>2</sub> subcell has the lowest individual subcell photocurrent and second lowest  $FF$  (69%). Lastly, the efficiency of the 3Js shown in Figure 7(c) illustrates much higher performance of the LMM 3J over the LM and CuInSe<sub>2</sub> 3Js with a maximum efficiency of 44% under 750 suns' illumination. The LM and CuInSe<sub>2</sub> 3Js peak at 40.5% and 39.6% for 750 suns, respectively. Although the efficiency of each 3J begins to degrade close to 1000 suns due to intrinsic semiconductor series resistance effects, the CuInSe<sub>2</sub> device degrades the least up to 3000 suns and surpasses the performance of the LM device.

The results of Figure 8 imply that all three of the 3Js explored in this study may have difficulty operating under concentrated illuminations of over 1000x in CPV systems. This represents an inherent limitation in  $FF$  and efficiency as a function of concentration based on tunnel junction and intrinsic semiconductor resistances. It is also important to note that the properties of epitaxial quality CuInSe<sub>2</sub> have

been much less studied experimentally than III–V materials. Further work may result in improved material quality and therefore a higher 3J performance due to improvements in both  $V_{oc}$  and  $FF$ . Lastly, the simulated LMM performance does not quite reach nor surpass the world record [42] for a number of reasons. The primary one involves the conservative minority carrier lifetimes assumed in the modeling. Another reason is the possible beneficial effects of photon recycling within each subcell and luminescent coupling between subcells, both of which are not considered in the model. Other reasons include improvements in the ARC design (materials and layer thicknesses) and improvements in each subcell design such as graded doping layers.

## 5. Conclusions

The simulated performance metrics of the GaInAs LMM 3J, the Ge LM 3J, and the proposed CuInSe<sub>2</sub> 3J are studied

up to concentration ratios of 3000 suns at 300 K. For the LMM and CuInSe<sub>2</sub> 3J designs, the modeling takes into account the effects of threading dislocations on minority carrier lifetimes in the bottom subcell. Although the bandgap combination of the CuInSe<sub>2</sub> 3J is more optimal than the LM 3J, their performances are comparable as a result of the low fill factor of CuInSe<sub>2</sub> 3J cell. With respect to their respective bottom subcells, it is especially important to note that the Ge subcell FF (63%) is lower than the CuInSe<sub>2</sub> subcell FF (69%). This emphasizes the need for a substantially higher photocurrent in the 3J's subcell with the lowest FF. Overall, the LMM 3J clearly outperforms the LM 3J and the CuInSe<sub>2</sub> 3J, achieving an efficiency of 44% under 750 suns concentration as compared to 40.5% and 39.6%, respectively. The main reasons for this higher performance are the LMM 3J's GaInAs subcell FF of 80% and its higher V<sub>oc</sub>. However, a strong advantage of the CuInSe<sub>2</sub> 3J is the reduction of III–V semiconductor material over the LMM 3J by around 20%, leading to a lower cost of the cell.

## Conflict of Interests

The authors declare that there is no conflict of interests regarding the publication of this paper.

## Acknowledgments

The authors would like to thank the Photovoltaic Innovation Network funded by the National Science and Engineering Research Council of Canada, the Ontario Graduate Scholarship fund, CMC Microsystems for the licensing of TCAD Sentaurus, the Ministry of Research and Innovation in Ontario, the Canadian Foundation for Innovation, and Canada Research Chair programs for funding.

## References

- [1] National Renewable Energy Laboratory, "Best research-cell efficiencies," [http://www.nrel.gov/ncpv/images/efficiency\\_chart.jpg](http://www.nrel.gov/ncpv/images/efficiency_chart.jpg).
- [2] R. R. King, D. C. Law, K. M. Edmondson et al., "40% efficient metamorphic GaInP/GaInAs/Ge multijunction solar cells," *Applied Physics Letters*, vol. 90, pp. 183516-1-183516-3, 2007.
- [3] F. Dimroth, W. Guter, J. Schöne et al., "Metamorphic GaInP/GaInAs/Ge triple-junction solar cells with > 41 % efficiency," in *Proceedings of the 34th IEEE Photovoltaic Specialists Conference (PVSC '09)*, Philadelphia, Pa, USA, June 2009.
- [4] J. F. Geisz, S. R. Kurtz, M. W. Wanlass et al., "Inverted GaInP/(In)GaAs/InGaAs triple-junction solar cells with low-stress metamorphic bottom junctions," in *Proceedings of the 33rd IEEE Photovoltaic Specialists Conference (PVSC '08)*, San Diego, Calif, USA, May 2008.
- [5] D. Liao and A. Rockett, "Epitaxial growth of Cu(In,Ga)Se<sub>2</sub> on GaAs(110)," *Journal of Applied Physics*, vol. 91, no. 3, pp. 1978–1983, 2002.
- [6] *Sentaurus Device User Guide, Version G-2012.06*, Synopsys, Mountain View, Calif, USA, 2012.
- [7] F. Bouchard, A. Walker, and K. Hinzer, "Modeling a monocrystalline Cu(In,Ga)Se<sub>2</sub> single junction solar cell grown on a GaAs substrate," in *The Photonics North*, vol. 8915 of *Proceedings of SPIE*, Ottawa, Canada, 2013.
- [8] Z. Zhang, W. Witte, O. Kiowski, U. Lemmer, M. Powalla, and H. Holscher, "Influence of the Ga Content on the optical and electrical properties of CuIn<sub>1-x</sub>Ga<sub>x</sub>Se<sub>2</sub> thin-film solar cells," *IEEE Journal of Photovoltaics*, vol. 3, no. 2, pp. 823–827, 2013.
- [9] D. J. Schroeder, G. D. Berry, and A. A. Rockett, "Gallium diffusion and diffusivity in CuInSe<sub>2</sub> epitaxial layers," *Applied Physics Letters*, vol. 69, no. 26, pp. 4068–4070, 1996.
- [10] J. T. Heath, J. D. Cohen, W. N. Shafarman, D. X. Liao, and A. A. Rockett, "Effect of Ga content on defect states in CuIn<sub>1-x</sub>Ga<sub>x</sub>Se<sub>2</sub> photovoltaic devices," *Applied Physics Letters*, vol. 80, no. 24, pp. 4540–4542, 2002.
- [11] D. J. Schroeder, J. L. Hernandez, G. D. Berry, and A. A. Rockett, "Hole transport and doping states in epitaxial CuIn<sub>1-x</sub>Ga<sub>x</sub>Se<sub>2</sub>," *Journal of Applied Physics*, vol. 83, no. 3, pp. 1519–1526, 1998.
- [12] Y. M. Strzhemechny, P. E. Smith, S. T. Bradley et al., "Near-surface electronic defects and morphology of CuIn<sub>1-x</sub>Ga<sub>x</sub>Se<sub>2</sub>," *Journal of Vacuum Science and Technology B: Microelectronics and Nanometer Structures*, vol. 20, no. 6, pp. 2441–2448, 2002.
- [13] R. Herberholz, V. Nadenau, U. Rühle, C. Köble, H. W. Schock, and B. Dimmler, "Prospects of wide-gap chalcopyrites for thin film photovoltaic modules," *Solar Energy Materials and Solar Cells*, vol. 49, no. 1–4, pp. 227–237, 1997.
- [14] U. Rau, A. Jasenek, H. W. Schock, F. Engelhardt, and T. Meyer, "Electronic loss mechanisms in chalcopyrite based heterojunction solar cells," *Thin Solid Films*, vol. 361, pp. 298–302, 2000.
- [15] G. Hanna, A. Jasenek, U. Rau, and H. W. Schock, "Influence of the Ga-content on the bulk defect densities of Cu(In,Ga)Se<sub>2</sub>," *Thin Solid Films*, vol. 387, no. 1-2, pp. 71–73, 2001.
- [16] A. Zakaria, R. R. King, M. Jackson, and M. S. Goorsky, "Comparison of arsenide and phosphide based graded buffer layers used in inverted metamorphic solar cells," *Journal of Applied Physics*, vol. 112, no. 2, Article ID 024907, 2012.
- [17] J. F. Geisz, S. Kurtz, M. W. Wanlass et al., "High-efficiency GaInP/GaAs/InGaAs triple-junction solar cells grown inverted with a metamorphic bottom junction," *Applied Physics Letters*, vol. 91, no. 2, Article ID 023502, 2007.
- [18] "Semiconductors on NSM," <http://www.ioffe.rssi.ru/SVA/NSM/Semicond/index.html>.
- [19] A. W. Walker, O. Thériault, M. Wilkins, J. F. Wheeldon, and K. Hinzer, "Nonlocal tunneling models and the simulation of tunnel junction limited multi-junction solar cells under concentration," *IEEE Journal of Selected Topics in Quantum Electronics: Numerical Simulation of Optoelectronic Devices*, vol. 19, no. 5, pp. 1–8, 2013.
- [20] J. F. Wheeldon, C. E. Valdivia, A. W. Walker et al., "Performance comparison of AlGaAs, GaAs and InGaP tunnel junctions for concentrated multijunction solar cells," *Progress in Photovoltaics: Research and Applications*, vol. 19, no. 4, pp. 442–452, 2011.
- [21] J. J. Schermer, G. J. Bauhuis, P. Mulder et al., "High rate epitaxial lift-off of InGaP films from GaAs substrates," *Applied Physics Letters*, vol. 76, no. 15, pp. 2131–2133, 2000.
- [22] A. W. Walker, O. Thériault, J. F. Wheeldon, and K. Hinzer, "The effects of absorption and recombination on quantum dot multi-junction solar cell efficiency," *IEEE Journal of Photovoltaics*, vol. 3, no. 3, pp. 1118–1124, 2013.
- [23] A. W. Walker, *Bandgap engineering of multi-junction solar cells using nanostructures for enhanced performance under concentration [Ph.D. Dissertation]*, Department of Physics, University of Ottawa, Ottawa, Canada, 2013.

- [24] W. N. Shafarman and L. Stolt, *Handbook of Photovoltaic Science and Engineering*, John Wiley & Sons, New York, NY, USA, 2003.
- [25] I. Vurgaftman, J. R. Meyer, and L. R. Ram-Mohan, "Band parameters for III-V compound semiconductors and their alloys," *Journal of Applied Physics*, vol. 89, no. 11 I, pp. 5815–5875, 2001.
- [26] T. Minemoto, T. Matsui, H. Takakura et al., "Theoretical analysis of the effect of conduction band offset of window/CIS layers on performance of CIS solar cells using device simulation," *Solar Energy Materials and Solar Cells*, vol. 67, no. 1-4, pp. 83–88, 2001.
- [27] S. H. Song, K. Nagaich, E. S. Aydil, R. Feist, R. Haley, and S. A. Campbell, "Structure optimization for a high efficiency CIGS solar cell," in *Proceedings of the 35th IEEE Photovoltaic Specialists Conference (PVSC '10)*, pp. 2488–2492, June 2010.
- [28] M. Gloeckler, A. L. Fahrenbruch, and J. R. Sites, "Numerical modeling of CIGS and CdTe solar cells: setting the baseline," in *Proceedings of the 3rd World Conference on Photovoltaic Energy Conversion*, pp. 491–494, Osaka, Japan, May 2003.
- [29] A. W. Haas, J. R. Wilcox, J. L. Gray, and R. J. Schwartz, "Design of a GaInP/GaAs tandem solar cell for maximum daily, monthly, and yearly energy output," *Journal of Photonics for Energy*, vol. 1, no. 1, Article ID 018001, 2011.
- [30] M. Sotoodeh, A. H. Khalid, and A. A. Rezazadeh, "Empirical low-field mobility model for III-V compounds applicable in device simulation codes," *Journal of Applied Physics*, vol. 87, no. 6, pp. 2890–2900, 2000.
- [31] S. Shirakata and T. Nakada, "Photoluminescence and time-resolved photoluminescence in Cu(In, Ga)Se<sub>2</sub> thin films and solar cells," *Physica Status Solidi C: Current Topics in Solid State Physics*, vol. 6, no. 5, pp. 1059–1062, 2009.
- [32] N. M. Haegel, S. E. Williams, C. L. Frenzen, and C. Scandrett, "Minority carrier lifetime variations associated with misfit dislocation networks in heteroepitaxial GaInP," *Semiconductor Science and Technology*, vol. 25, no. 5, Article ID 055017, 2010.
- [33] P. D. Paulson, R. W. Birkmire, and W. N. Shafarman, "Optical characterization of CuIn<sub>1-x</sub>Ga<sub>x</sub>Se<sub>2</sub> alloy thin films by spectroscopic ellipsometry," *Journal of Applied Physics*, vol. 94, no. 2, pp. 879–888, 2003.
- [34] S. Adachi, *Properties of Semiconductor Alloys: Group-IV, III-V and II-VI Semiconductors*, chapter 10, John Wiley & Sons, 2009.
- [35] K.-H. Goetz, D. Bimberg, H. Juergensen et al., "Optical and crystallographic properties and impurity incorporation of Ga<sub>x</sub>In<sub>1-x</sub>As (0.44 < x < 0.49) grown by liquid phase epitaxy, vapor phase epitaxy, and metal organic chemical vapor deposition," *Journal of Applied Physics*, vol. 54, no. 8, pp. 4543–4552, 1983.
- [36] E. D. Palik, *Handbook of Optical Constants of Solids*, vol. 1, chapter 18, Academic Press, San Diego, Calif, USA, 1998.
- [37] J. Piprek, *Semiconductor Optoelectronic Devices: Introduction to Physics and Simulation*, chapter 3, Academic Press, San Diego, Calif, USA, 2003.
- [38] M. S. Lundstrom, M. E. Klausmeier-Brown, M. R. Melloch, R. K. Ahrenkiel, and B. M. Keyes, "Device-related material properties of heavily doped gallium arsenide," *Solid-State Electronics*, vol. 33, no. 6, pp. 693–704, 1990.
- [39] T. Ohori, S. Ohkubo, K. Kasai, and J. Komeno, "Effect of threading dislocations on mobility in selectively doped heterostructures grown on Si substrates," *Journal of Applied Physics*, vol. 75, no. 7, pp. 3681–3683, 1994.
- [40] C. L. Andre, D. M. Wilt, A. J. Pitera, M. L. Lee, E. A. Fitzgerald, and S. A. Ringel, "Impact of dislocation densities on n +/p and p +/n junction GaAs diodes and solar cells on SiGe virtual substrates," *Journal of Applied Physics*, vol. 98, no. 1, Article ID 014502, 2005.
- [41] M. M. Wilkins, A. Boucherif, R. Beal et al., "Multijunction solar cell designs using silicon bottom subcell and porous silicon compliant membrane," *IEEE Journal of Photovoltaics*, vol. 3, no. 3, pp. 1125–1131, 2013.
- [42] M. A. Green, K. Emery, Y. Hishikawa, W. Warta, and E. D. Dunlop, "Solar cell efficiency tables (version 42)," *Progress in Photovoltaics: Research and Applications*, vol. 21, no. 5, pp. 827–837, 2013.



**Hindawi**

Submit your manuscripts at  
<http://www.hindawi.com>

